

TABLE OF CONTENTS

	Page
ACKNOWLEDGMENT	iii
ABSTRACT (ENGLISH)	v
ABSTRACT (THAI)	vii
LIST OF TABLES	xiv
LIST OF ILLUSTRATIONS	xvi
ABBREVIATIONS AND SYMBOLS	xxv
CHAPTER 1 INTRODUCTION	1
1.1 Ferroelectrics	1
1.2 Relaxor ferroelectrics	5
1.2.1 Introduction	5
1.2.2 Relaxor ferroelectric behavior	5
1.2.3 Relaxor ferroelectric modeling	10
1.3 Perovskite materials	15
1.3.1 Introduction	15
1.3.2 Crystal structure	15
1.3.3 Tolerance factor and phase stability	18
1.3.4 Columbite-(wolframite) Precursor Method	22
1.4 Morphotropic Phase Boundary (MBP) in normal and relaxor ferroelectric Solid solution	23

	Page
1.4.1 Introduction	23
1.4.2 Stabilization of the perovskite phase of PZN ceramic solid solutions	26
1.4.3 Characteristic features of ferroelectric Pb (Ni _{1/3} Nb _{2/3})O ₃ -Pb(Zr _x Ti _{1-x})O ₃ ceramics	34
CHAPTER 2 PURPOSES OF THE RESEARCH	40
CHAPTER 3 EXPERIMENTAL PROCEDURES	42
3.1 Powder preparation	42
3.1.1 Preparation of the PZN-PZT system	46
3.1.1.1 Solid-state mixed oxide method	47
3.1.1.2 Columbite-wolframite precursors method	48
3.1.2 Preparation of PNN-PZT powders	52
3.1.3 Preparation of PNN-PZN-PZT powders	53
3.2 Ceramic processing	57
3.3 Structure characterization	59
3.3.1 X-ray diffraction (XRD)	59
3.3.2 Scanning electron microscopy (SEM)	59
3.3.3 Transmission electron microscopy (TEM)	60

	Page
3.4 Property measurement	60
3.4.1 Electric field-polarization hysteresis	60
3.4.2 Dielectric measurements in normal atmosphere	61
3.4.3 Piezoelectric coefficients and electromechanical coupling factors	64
CHAPTER 4 INFLUENCE OF PROCESSING CONDITIONS ON THE PHASE TRANSITION AND FERROELECTRIC PROPERTIES OF $x\text{Pb}(\text{Zn}_{1/3}\text{Nb}_{2/3})\text{O}_3 - (1-x)\text{Pb}(\text{Zr}_{1/2}\text{Ti}_{1/2})\text{O}_3$ CERAMICS	65
4.1 Introduction	66
4.2 Experimental procedure	68
4.3 Results and discussion	69
4.3.1 Perovskite phase formation and the MPB	69
4.3.2 Effect of sintering temperature and post-sinter annealing	78
4.3.3 Effect of processing method on the phase transformation	83
4.4 Conclusion	86

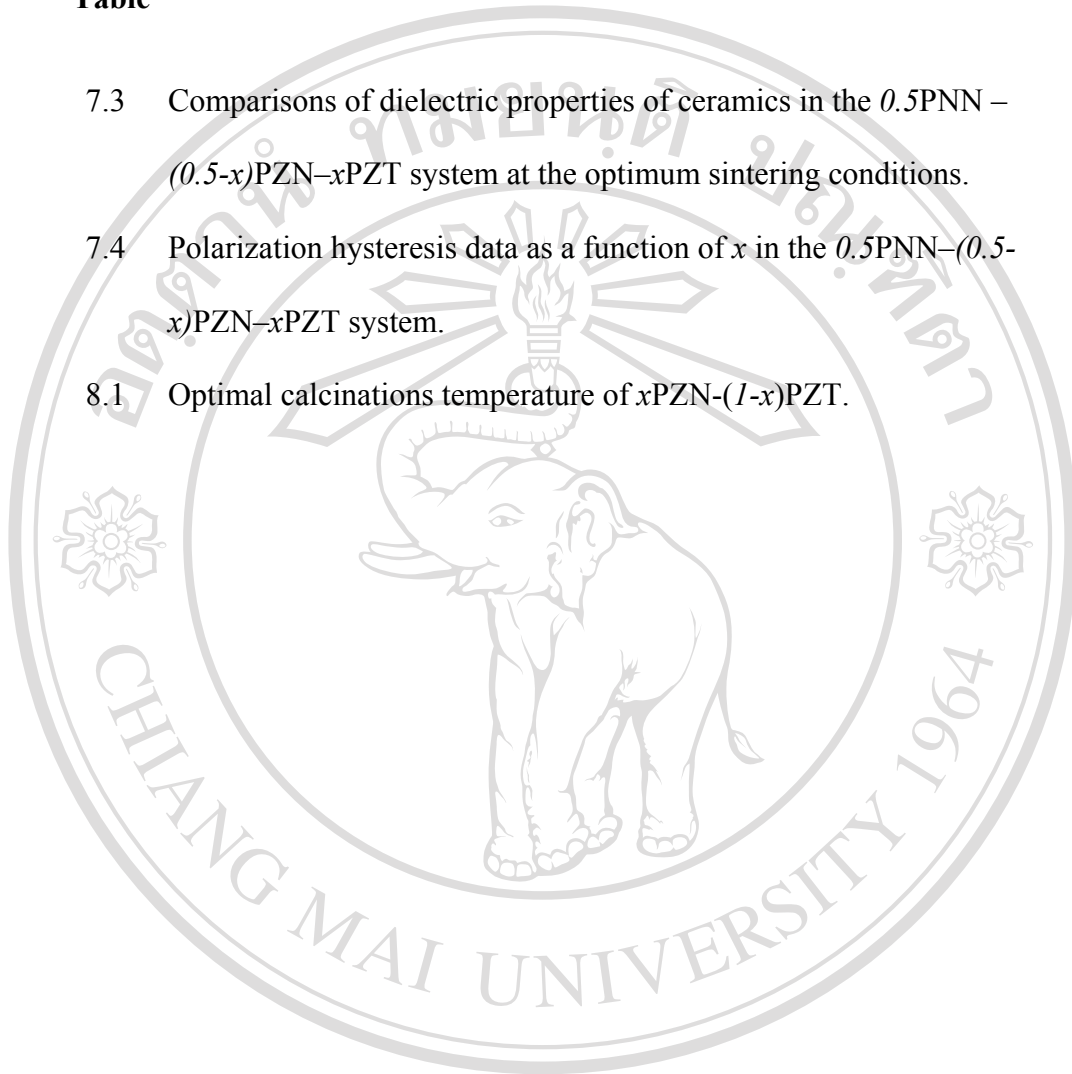
	Page
CHAPTER 5 DIELECTRIC PROPERTIES AND MORPHOTROPIC	88
PHASE BOUNDARY IN THE $x\text{Pb}(\text{Zn}_{1/3}\text{Nb}_{2/3})\text{O}_3 - (1-x)$	
$\text{Pb}(\text{Zr}_{0.5}\text{Ti}_{0.5})\text{O}_3$ PSEUDO-BINARY SYSTEM	
5.1 Introduction	89
5.2 Experimental Procedure	90
5.3 Results and discussion	92
5.3.1 Perovskite phase formation and microstructure	92
5.3.2 Dielectric behavior	97
5.3.3 The morphotropic phase boundary	105
5.3.4 Piezoelectric properties	110
5.3.5 The PZN–PZT phase diagram	112
5.4 Conclusion	113
CHAPTER 6 THE MORPHOTROPIC PHASE BOUNDARY AND	115
DIELECTRIC PROPERTIES OF $x\text{Pb}(\text{Zr}_{1/2}\text{Ti}_{1/2})\text{O}_3 - (1-x)$	
$\text{Pb}(\text{Ni}_{1/3}\text{Nb}_{2/3})\text{O}_3$ PEROVSKITE SOLID SOLUTION	
6.1 Introduction	116
6.2 Experimental procedure	119
6.3 Results and discussion	121
6.3.1 Crystal structure and phase transition studies	121
6.3.2 Dielectric properties	124
6.3.3 Phase diagram of $\text{Pb}(\text{Zr}_{1/2}\text{Ti}_{1/2})\text{O}_3 - \text{Pb}(\text{Ni}_{1/3}\text{Nb}_{2/3})\text{O}_3$	134
6.4 Conclusion	134

	Page
CHAPTER 7 PEROVSKITE PHASE FORMATION AND FERRO-ELECTRIC PROPERTIES OF THE PNN-PZN-PZT TERNARY SYSTEM	137
7.1 Introduction	138
7.2 Experimental procedure	140
7.3 Results and discussion	142
7.3.1 Perovskite phase development	142
7.3.2 Dielectric properties	150
7.3.3 Ferroelectric and Electrostrictive properties	158
7.3.4 TEM characterization	160
7.4 Conclusion	166
CHAPTER 8 CONCLUSIONS AND FUTUER WORK	167
8.1 Conclusions	167
8.1.1 PZN-PZT system	167
8.1.2 PNN-PZT system	170
8.1.3 PNN-PZN-PZT system	171
8.2 Future work	176
REFERENCES	181
VITA	186

LIST OF TABLES

Table		Page
1.1	Property difference between relaxor and normal perovskite ferroelectrics.	9
1.2	Composition and properties of PZN based ceramics.	29
3.1	Specifications of the component oxide powders used in this study.	44
4.1	Post-sinter annealing effects on the remanent polarization P_r and saturation polarization P_s in x PZN– $(1-x)$ PZT ceramics sintered at 1175°C for 2 hours and annealed at 1250°C for 6 hours.	80
5.1	Comparison of the dielectric properties of x PZN– $(1-x)$ PZT ceramics prepared by the conventional mixed-oxide and columbite methods.	99
5.2	Comparison of the piezoelectric properties observed in this study with previous studies.	112
6.1	Dielectric properties of x PZT– $(1-x)$ PNN ceramics	129
7.1	Perovskite phase development during calcinations and sintering process of 0.5 PNN– $(0.5-x)$ PZN– x PZT system (The first two rows indicate the data in calcined powders and the rest rows are data from sintering of powders calcined at 950 °C).	145
7.2	Comparison of the calculated average B-site ionic radii, the crystal structure, and lattice parameters derived from XRD data.	149

Table	Page
7.3 Comparisons of dielectric properties of ceramics in the $0.5\text{PNN} - (0.5-x)\text{PZN}-x\text{PZT}$ system at the optimum sintering conditions.	156
7.4 Polarization hysteresis data as a function of x in the $0.5\text{PNN}-(0.5-x)\text{PZN}-x\text{PZT}$ system.	163
8.1 Optimal calcinations temperature of $x\text{PZN}-(1-x)\text{PZT}$.	169



ลิขสิทธิ์มหาวิทยาลัยเชียงใหม่
Copyright © by Chiang Mai University
All rights reserved

LIST OF ILLUSTRATIONS

Figure		Page
1.1	A typical ferroelectric hysteresis loop.	4
1.2	Curie-Weiss plot for a barium strontium titanate composition.	4
1.3	Differences between ordered and disordered $\text{Pb}(\text{Sc}_{1/2}\text{Ta}_{1/2})\text{O}_3$.	13
1.4	Various relaxor perovskite combinations and their classification based on short and long range ordering.	14
1.5	Two alternative representations of the perovskite (ABO_3) structure.	17
1.6	Structure-Filed map for various perovskite materials based on electronegativity difference and tolerance factor.	20
1.7	Ternary diagram depicting MPBs in PZT and relaxor-PZT systems for piezoelectric ceramics.	25
1.8	Relative concentration of the rhombohedral phase with respect to the tetragonal phase as a function of PZT content.	30
1.9	TEM micrographs of $(1-x)\text{PZN} - x\text{PZT}$ ceramics: (a) $x = 0.4$, (b) $x = 0.5$, (c) $x = 0.6$, (d) $x = 0.7$, showing the evolution of the tetragonal domains (Tet. Domain) and the rhombohedral domains (Rh. Domain).	31
1.10	SEM micrographs of $\text{Pb}_x((\text{Zn}_{1/3}\text{Nb}_{2/3})_{0.5}(\text{Zr}_{0.47}\text{Ti}_{0.53})_{0.5})\text{O}_3$ ceramics: (A) free surface with $x = 0.98$, (B) fracture surface with $x = 0.98$, (C) free surface with $x = 1.01$, and (D) free surface with $x = 1.03$.	33

Figure	Page
1.11 Temperature dependence of the dielectric constant and loss for PNNZT ceramics.	35
1.12 (a) Room temperature dielectric hysteresis loops for PNNZT ceramics (b) Room temperature field induced strain for PNNZT ceramics.	37
1.13 Permittivity versus temperature curves for the 26 mol% PZ composition.	38
1.14 Proposed phase diagram for a PNN–PZT system containing 40 mol% PNN, measured at 1 kHz ("F" denotes normal ferroelectric, "R" denotes relaxor ferroelectric, and "P" denotes paraelectric).	38
3.1 Mixed and Calcination Processes (MCP) for powder preparation.	45
3.2 The double crucible technique.	46
3.3 The processing flow chart for the PZN-PZT powder.	50
3.4 Columbite-wolframite precursor for binary solid solution PZN-PZT.	51
3.5 Columbite-wolframite precursor for binary solid solution PZT-PNN.	55
3.6 Columbite-wolframite precursor for binary solid solution, PNN-PZN-PZT.	56
3.7 Schematic diagrams showing the double-inverted crucible technique.	58
3.8 Schematic diagram of sample holder for high temperature dielectric measurement.	63

Figure	Page
4.1 XRD patterns for $0.3\text{PZN} - 0.7\text{PZT}$ ceramics calcined at varies temperatures for 4 hours. (a) columbite method ; (b) conventional method.	72
4.2 Percentage of perovskite phase as a function of calcination temperature for $x\text{PZN} - (1-x)\text{PZT}$ ceramics: (a) columbite method; (b) conventional method.	73
4.3 XRD patterns for $x\text{PZN} - (1-x)\text{PZT}$ ceramics sintered at 1200°C for 2 hours : (a) columbite method ; (b) conventional method.	75
4.4 Close examination of the (002) peaks shown in Fig. 4.2 (a) columbite method; (b) conventional method.	76
4.5 Individual x-ray diffraction (002) peak for the tetragonal ($F_{\text{T}(002)}$), $F_{\text{T}(200)}$) and Rhombohedral($F_{\text{R}(200)}$) phase for difference methods, (a) $0.2\text{PZN}-0.8\text{PZT}$ prepared by columbite method, (b) $0.3\text{PZN}-0.7\text{PZT}$ prepared by columbite method. (c) $0.2\text{PZN}-0.8\text{PZT}$ prepared by conventional method. (d) $0.3\text{PZN}-0.7\text{PZT}$ prepared by conventional method.	77
4.6 Room temperature P-E hysteresis as a function of sintering temperature for $0.2\text{PZN} - 0.8\text{PZT}$: (a) columbite method; (b) conventional method.	81

Figure	Page
4.7 Effect of post-sinter annealing on the P-E hysteresis for $0.1\text{PZN} - 0.9\text{PZT}$ ceramics: (●) sintered at 1250°C , (○) sintered at 1175°C and annealed at 1250°C for 6 hours: (a) columbite method, (b) conventional method.	82
4.8 Effect of composition (x) on the P-E hysteresis loops for $x\text{PZN} - (1-x)\text{PZT}$ processed at the optimum processing conditions: (a) columbite method; (b) conventional method.	84
4.9 Variation of remanent polarization P_r and coercive field E_c with composition for $x\text{PZN} - (1-x)\text{PZT}$ ceramics: (a) remanent polarization; (b) coercive field.	85
5.1 XRD spectra of $0.5\text{PZN}-0.5\text{PZT}$ powder calcined at various temperatures for 4 hours. (a) the conventional mixed-oxide method; and (b) the columbite method.	94
5.2 Perovskite phase content in $0.5\text{PZN}-0.5\text{PZT}$ powders calcined at different temperatures.	95
5.3 SEM examination of the grain morphology in $x\text{PZN}-(1-x)\text{PZT}$; $x = 0.1-0.5$ ceramics sintered at optimum sintering condition: (a), (c) and (e) prepared by conventional method; (b),(d) and (f) prepared by columbite method.	96

Figure	Page
5.4 Relative permittivity versus temperature curves for the x PZN-($1-x$)PZT ceramics. The frequency used for the measurement is 1 kHz:(a) conventional method; and (b) columbite method.	100
5.5 Phase transitions detected from the ϵ_r versus T curves in ceramics prepared via the columbite method. (a) 0.3PZN-0.7PZT ceramic at 1 kHz; and (b) 0.5PZN-0.5PZT ceramic at 0.1, 1, 10 and 100 kHz. (c) 0.6PZN- 0.4PZT ceramic at 0.1, 1, 10 and 100 kHz.	102
5.6 Variation of T_{\max} with increasing PZN content x in the x PZN-($1-x$)PZT system.	103
5.7 The $\log\left[\left(\frac{\epsilon_{r\max}}{\epsilon}\right)-1\right]$ vs. $\log(T - T_{\max})$ plots for (a) 0.1PZN-0.9PZT and (b) 0.5PZN-0.5PZT.	104
5.8 Coercive field (E_c) and relative permittivity versus x in x PZN-($1-x$)PZT ceramics showing the presence of MPB at $x \approx 0.25$.	106
5.9 Raman spectroscopy curves for x PZN-($1-x$)PZT ceramics prepared by (a) conventional and (b) columbite method.	107
5.10 TEM micrographs of the 0.1PZN-0.9PZT ceramic;(a-d) shows the evolution of the tetragonal domains.	108
5.11 TEM micrographs of the 0.5 PZN-0.5PZT ceramic; (a-d) shows the evolution of the rhombohedral domains.	109

Figure	Page
5.12 Piezoelectric coefficient d_{33} as a function of sintering temperature for x PZN-(1- x)PZT ceramics prepared via columbite method.	111
5.13 Piezoelectric properties of d_{33} and k_p in ceramics prepared with optimized processing conditions.	111
5.14 The proposed phase diagram for the Pb(Zn _{1/3} Nb _{2/3})O ₃ -Pb(Zr _{0.5} Ti _{0.5})O ₃ pseudo-binary solid solution system. The solid circles represent data points obtained from the present study, the open circles represent data taken from reference 21.	114
6.1 Compositions studied in the Pb(Ni _{1/3} Nb _{2/3})O ₃ -PbZrO ₃ -PbTiO ₃ ternary system.	118
6.2 X-ray diffraction patterns at room temperature for x PZT - (1- x)PNN ceramics.	122
6.3 X-ray pattern of the (200) and (220) peak of x PZT - (1- x)PNN, $x = 0.4 - 0.6$ ceramics.	123
6.4 X-ray pattern of the (111) and (200) peak of x PZT - (1- x)PNN, $x = 0.6 - 0.9$ ceramics.	123
6.5 Temperature dependence of relative permittivity ϵ_r for x PZT - (1- x)PNN, $x = 0.4 - 0.9$ ceramics.	127
6.6 Temperature dependence of relative permittivity ϵ_r for x PZT - (1- x)PNN, a: $x = 0.5$, b: $x = 0.7$ and c: $x = 0.8$ ceramics is shown.	128

Figure	Page
6.7 T_{max} , Calculated T_{max} and Maximum ϵ_r as a function of composition x at 10 kHz.	131
6.8 Dependence of $\text{Log}[(\epsilon_m/\epsilon)-1]$ with $\text{Log}(T-T_{max})$ for $x\text{PZT} - (1-x)\text{PNN}$, $x = 0.4-0.9$ ceramics.	132
6.9 Dependence of γ and degree of diffuseness (δ_γ) for $x\text{PZT} - (1-x)\text{PNN}$, $x = 0.4-0.9$ ceramics.	133
6.10 Phase diagram of $x\text{PZT} - (1-x)\text{PNN}$, $x = 0.4-0.9$ binary system determined from room temperature XRD, Raman spectra and dielectric spectra as a function of temperature. The symbols refer to: ■ = the transition temperature from ferroelectric (F_R , F_T and F_{PC}) to relaxor (P_C); ● = the transition temperature from ferroelectric state (F_R , F_T and F_{PC}) to paraelectric state (cubic); ▲ = the transition temperature from rhombohedral (F_R) to tetragonal (F_T).	136
7.1 Powder XRD patterns of a stoichiometric composition of $0.5\text{PNN} - (0.5-x)\text{PZN} - x\text{PZT}$ ceramics: (a) Calcined at 900°C for 4h with $20^\circ\text{C}/\text{min}$ heating rate; (b) Calcined at 950°C for 2h with $20^\circ\text{C}/\text{min}$ heating rate. Pyrochlore phase indicated with *.	144
7.2 XRD patterns of $0.5\text{PNN} - (0.5-x)\text{PZN} - x\text{PZT}$ ceramics at the optimum sintering conditions.	146

Figure	Page
7.3 XRD patterns of the (220) peak of $0.5\text{PNN}-(1-x)\text{PZN}-x\text{PZT}$ ceramic; a : $x = 0$, b: $x = 0.1$, c: $x = 0.3$, d: $x = 0.5$.	148
7.4 Relative permittivity and dissipation factor at 1kHz for $0.5\text{PNN}-(0.5-x)\text{PZN}-x\text{PZT}$; a : $x = 0$, b : $x = 0.1$ Dielectric data for difference sintering temperature is shown. C: $x = 0.3$, d : $x = 0.5$. Dielectric data for difference sintering temperature is shown.	152
7.5 Relative permittivity and dissipation factor of $0.5\text{PNN}-(0.5-x)\text{PZN}-x\text{PZT}$ ceramics prepared at the optimum sintering conditions a: $x = 0.0$, ceramics sintered at 1150°C for 2h; b: $x = 0.1$, ceramics sintered at 1200°C for 2h; c: $x = 0.3$, ceramics sintered at 1200°C for 2h; c: $x = 0.5$, ceramics sintered at 1250°C for 2h;	154
7.6 T_m , Calculated T_m and room temperature relative permittivity as a function of composition x at 1 kHz.	158
7.7 Room temperature polarization vs. electric field hysteresis loop of $0.5\text{PNN}-(0.5-x)\text{PZN}-x\text{PZT}$ ceramic at the optimum sintering conditions.	161
7.8 Temperature dependence of the $P-E$ hysteresis of $0.5\text{PNN}-(0.5-x)\text{PZN}-x\text{PZT}$ ceramics at optimum sintering conditions, compositions $x = 0.0$ and $x = 0.3$ are shown.	162

Figure	Page
7.9 Induced strain vs. electric field butterfly loops for $0.5\text{PNN} - (0.5-x)\text{PZN} - x\text{PZT}$ ceramics at the optimum sintering conditions.	164
7.10 TEM micrographs of the $0.5\text{PNN} - (0.5-x)\text{PZN} - x\text{PZT}$ ceramics; show the evolution of the micro-nano domain transition.(a) $x = 0.0$, showing nano-domain.(b) $x = 0.5$ showing micro-domain.	165
8.1 Schematic representation of piezoelectric coefficient (d_{33}) as a function of transition temperature for this study compared with other piezoelectric materials. Modified from Seung-Eek Park and Thomas R.Throut.	173
8.2 Relative permittivity as a function of transition temperature (T_m) for this study compared with other piezoelectric ceramics. Modified from Seung-Eek Park and Thomas R.Throut.	174
8.3 Transition temperatures as a function of the perovskite tolerance factors of the MPB composition in this system compared with other MPB composition. Modified from Eitel <i>et.al.</i>	175
8.4 Electromechanical coupling factors, k_p , versus the average B-site ionic size of the MPB composition. Modified from Yamashita and Ichinose.	176
8.5 tolerance factor and crystal structure in PNN – PZN – PZT system.	178

ABBREVIATIONS AND SYMBOLS

a	lattice parameter a
ac	alternating current
A	area
b	lattice parameter b
C	Curie-Weiss constant
c	capacitance
dc	direct current
d_{ij}	piezoelectric coefficients
DMM	Digital Multimeters
DPT	Diffuse Phase Transition
E	electric field ($V m^{-1}$); strain
ΔEN	electronegativity
E_c	Coercive field
e	electron charge
f	frequency
f_a	anti-resonance frequency
f_r	resonance frequency
F	normal ferroelectric
I_{perov}	maximum intensity of perovskite phase
I_{pyro}	maximum intensity of pyrochlore phase
I_{PbO}	maximum intensity of lead oxide phase

K_{α}	radiation of K series
k_{ij}	electromechanical coupling
LCR	Inductance/Capacitance/Resistance
MW	molecular weight
MPB	Morphotropic Phase Boundaries
MCP	Mixed and Calcination Processes
P-E	polarization versus electric field
P_s	spontaneous polarization
P_r	remanent polarization
P	paraelectric
PVA	poly(vinyl alcohol)
r_i	radius of atom
R	relaxor ferroelectric
Rh. Domain	rhombohedral domains
SEM	scanning electron microscopy
S_{ij}	field-induced strain
TEM	transmission electron microscopy
T_0	Curie-Weiss temperature
T_{RT}	Rhombohedral to Tetragonal temperature
T_{max}	temperature at maximum permittivity
T_m	Transition temperature
T_c	Curie point
Tet. Domain	tetragonal domains

t	thickness; tolerance factor
$\tan \delta$	loss tangent
V	voltage; volume
XRD	x-ray diffraction
X_{A-O}	electronegativity differences of cation A and oxygen
X_{B-O}	electronegativity differences of cation B and oxygen
δ	diffuseness parameter
ϵ	real part of the permittivity
ϵ_0	permittivity of free space
ϵ_r	relative permittivity
ϵ_{\max}	the permittivity at T_{\max}
γ	critical exponent
ω	driving frequency

ลิขสิทธิ์มหาวิทยาลัยเชียงใหม่
 Copyright © by Chiang Mai University
 All rights reserved